

Nanoscale Patterning of Extracellular Matrix Alters Endothelial Function under Shear Stress

Karina H. Nakayama,^{†,‡,§} Vinay N. Surya,^{†,||} Monica Gole,[§] Travis W. Walker,[⊥] Weiguang Yang,[#] Edwina S. Lai,^{||} Maggie A. Ostrowski,^{||} Gerald G. Fuller,^{||} Alexander R. Dunn,^{†,||} and Ngan F. Huang^{*,†,‡,§}

[†]Stanford Cardiovascular Institute, Stanford, California 94305, United States

[‡]Department of Cardiothoracic Surgery, Stanford School of Medicine, Stanford, California 94305, United States

[§]Veterans Affairs Palo Alto Health Care System, Palo Alto, California 94304, United States

^{||}Department of Chemical Engineering, Stanford University School of Engineering, Stanford, California 94305, United States

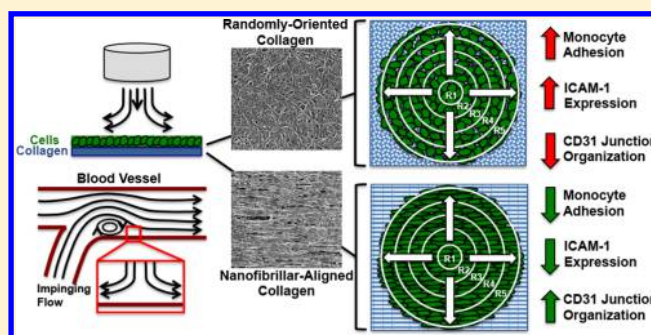
[⊥]Department of Chemical Engineering, Oregon State University, Corvallis, Oregon 97331, United States

[#]Department of Pediatrics, Stanford School of Medicine, Stanford, California 94305, United States

S Supporting Information

ABSTRACT: The role of nanotopographical extracellular matrix (ECM) cues in vascular endothelial cell (EC) organization and function is not well-understood, despite the composition of nano- to microscale fibrillar ECMs within blood vessels. Instead, the predominant modulator of EC organization and function is traditionally thought to be hemodynamic shear stress, in which uniform shear stress induces parallel-alignment of ECs with anti-inflammatory function, whereas disturbed flow induces a disorganized configuration with pro-inflammatory function. Since shear stress acts on ECs by applying a mechanical force concomitant with inducing spatial patterning of the cells, we sought to decouple the effects of shear stress using parallel-aligned nanofibrillar collagen films that induce parallel EC alignment prior to stimulation with disturbed flow resulting from spatial wall shear stress gradients. Using real time live-cell imaging, we tracked the alignment, migration trajectories, proliferation, and anti-inflammatory behavior of ECs when they were cultured on parallel-aligned or randomly oriented nanofibrillar films. Intriguingly, ECs cultured on aligned nanofibrillar films remained well-aligned and migrated predominantly along the direction of aligned nanofibrils, despite exposure to shear stress orthogonal to the direction of the aligned nanofibrils. Furthermore, in stark contrast to ECs cultured on randomly oriented films, ECs on aligned nanofibrillar films exposed to disturbed flow had significantly reduced inflammation and proliferation, while maintaining intact intercellular junctions. This work reveals fundamental insights into the importance of nanoscale ECM interactions in the maintenance of endothelial function. Importantly, it provides new insight into how ECs respond to opposing cues derived from nanotopography and mechanical shear force and has strong implications in the design of polymeric conduits and bioengineered tissues.

KEYWORDS: Nanofibrillar scaffold, collagen, endothelial cell, patterning, inflammation



The extracellular matrix (ECM) in which cells reside not only serves as a structural scaffolding structure, but also provides signaling cues derived from its topographical organization, biochemical composition, and rigidity.¹ In particular, the effect of nanotopographical ECM organization on vascular endothelial cell (EC) structure and function is not well-understood, despite the presence of nano- to microscale fibrillar ECM networks within blood vessels.^{2,3} Although parallel-aligned (anisotropic) ECMs have been shown to direct cytoskeletal reorganization along the axis of patterning for numerous cell types,^{4,5} the physiological modulator of EC orientation is traditionally thought to be hemodynamic shear stress.^{6,7} In straight segments of vessels, the ECs that line the innermost layer morphologically are parallel-aligned along the

direction of laminar blood flow. Functionally, these aligned ECs are protected from atherosclerotic lesion formation due to the suppressed activity of adhesion molecules on the cell surface, and thereby have weak binding to leukocytes in the lumen of the vessel.^{8–11} In contrast, at bends and branches of vessels where disturbed flow predominates, ECs adopt a disorganized cobblestone-like appearance and exhibit increased leukocyte adhesion and infiltration, making these regions more inflamed and prone to atherosclerotic lesion formation.¹⁰ Consequently,

Received: October 4, 2015

Revised: December 10, 2015

Published: December 16, 2015

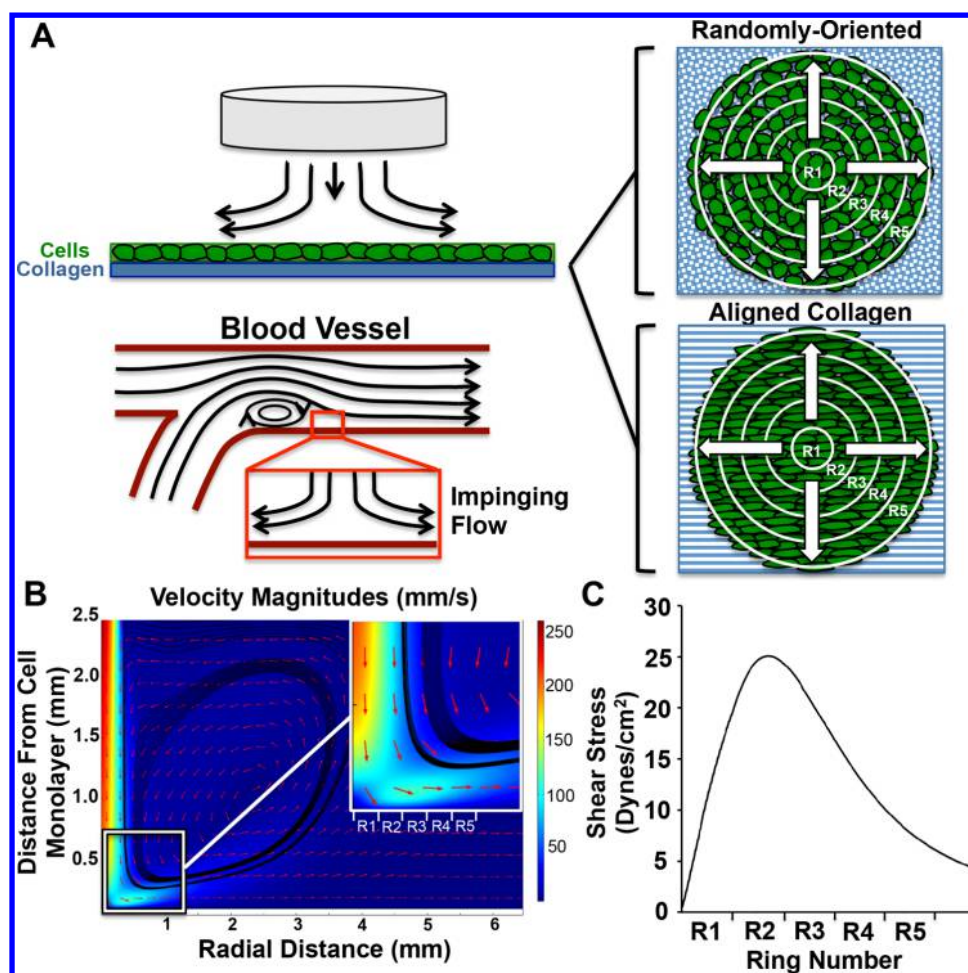


Figure 1. Characterization of the disturbed flow system. (A) Diagram of flow with a stagnation point, which creates spatial gradients in wall shear stress similar to those found at vessel bifurcations. Media flows downward from an orifice to a monolayer of ECs cultured on randomly oriented or aligned nanofibrillar collagen films. White circles show the concentric organization of the gradient rings and arrows show the radial direction of flow. (B) The velocity field is computed in COMSOL. Velocity magnitudes and directions are represented by colors and arrows, respectively. The velocity field is axisymmetric around the z -axis. Flow impinges the monolayer ($z = 0$) vertically from the orifice ($x = 0, z = 2.5$ mm). The flow profile across the five rings is shown in the magnified inset. (C) The wall shear stress magnitude across the five rings. Maximum wall shear is reached in R2.

parallel-aligned cellular patterning is an important indicator of endothelial health.¹² On the other hand, disorganized cellular organization is associated with increased risk of atherosclerosis, an inflammatory disease characterized by luminal narrowing and lesion formation within blood vessels^{8,13} that affects over 24 million people in the US.¹⁴

Given the intrinsic coupling of shear stress with endothelial patterning, the contribution of cell patterning to endothelial function has been difficult to disentangle from mechanical shear force. To address this limitation, we developed a platform to decouple shear stress from cell patterning using parallel-aligned nanofibrillar polymer films and real-time image analysis. By patterning ECs using aligned nanofibrillar films and then applying disturbed flow resulting from varying spatial wall shear stresses,¹⁵ we report an important contribution of nanoscale cues in regulating EC reorganization, motility, inflammatory function, and junctional organization, which has fundamental importance in understanding the development of atherosclerosis and has translational relevance in engineering vascular tissues.

We developed a platform to study EC response to complex shear stress conditions that oppose the direction of cell patterning. To induce parallel cell alignment, parallel-aligned

nanofibrillar films were generated by a shear-mediated extrusion process that induces collagen fibrillogenesis along the direction of extrusion. Primary human ECs were first patterned onto nanofibrillar collagen membranes (Figure S1a, Supporting Information) having randomly oriented (Figure S1b, Supporting Information) or aligned nanofibrils (Figure S1c, Supporting Information). On randomly oriented nanofibrillar collagen membranes, the ECs exhibited a disorganized morphology based on F-actin stress fiber assembly (Figure S1d, Supporting Information). In contrast, ECs cultured on aligned nanofibrillar collagen with 30–50 nm fibril diameters readily reorganized their actin cytoskeleton along the direction of the nanofibrils (Figure S1e, Supporting Information).

To examine how patterned ECs respond to spatially varying shear stress magnitudes and orientations, a custom-built flow cell device was suspended above the cell culture dish that dispensed cell culture media radially from the flow orifice onto a monolayer of ECs cultured on top of either parallel-aligned or randomly oriented nanofibrillar collagen films. The flow device mimicked disturbed flow by producing a stagnation point flow directly below the flow orifice (Figure 1A) and a well-controlled spatiotemporal wall shear stress profile.¹⁵ As validated by computational fluid dynamic modeling, the magnitude and

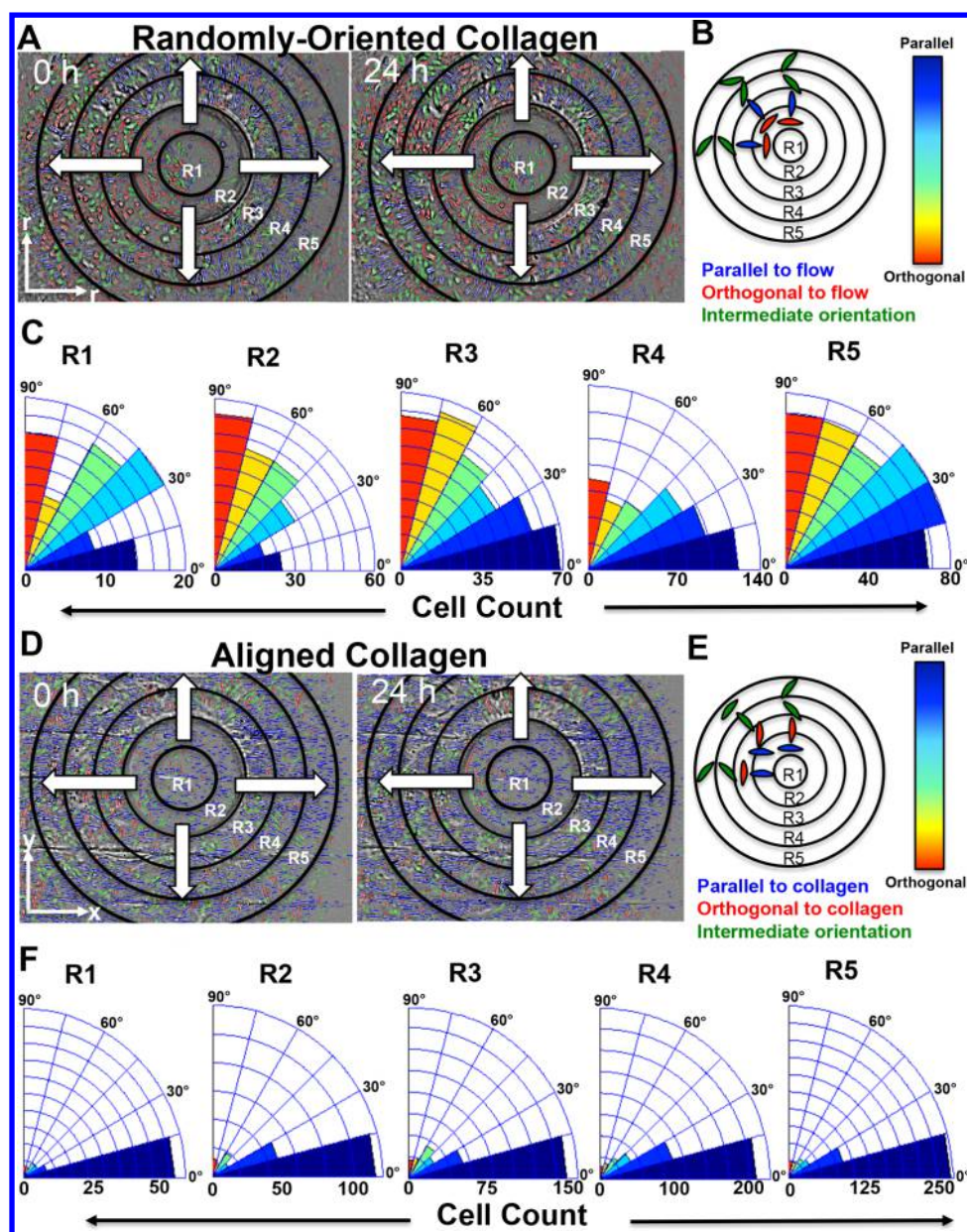


Figure 2. ECs remained oriented along the direction of aligned nanofibrils when exposed to spatially varying wall shear stress. (A) Spatial orientation of cells on randomly oriented collagen before (0 h) and after (24 h) exposure to disturbed flow. (B) Radial alignment of cells relative to the direction of shear stress is denoted by pseudocoloring. (C) Rose histograms show the distribution of angular alignment relative to a radial flow profile for each ring in polar coordinates. (D) Spatial orientation of cells on aligned collagen before (0 h) and after (24 h) exposure to disturbed flow. (E) The alignment of cells relative to the direction of the collagen fibrils is denoted by pseudocoloring. (F) Rose histograms show the distribution of angular alignment for each ring in Cartesian coordinates, relative to the nanofibril direction. Data shown are based on four samples per group out of all detectable cells in each ring.

direction of fluid velocity varied with respect to vertical (z -axis) and radial (x - and y -axes) distances from the flow orifice (Figure 1B). Once the velocity field was solved numerically, the shear stress experienced by the cell monolayer was calculated by multiplying the fluid viscosity with the wall shear stress at $z = 0$ (derivative of velocity with respect to z). Although the fluid velocity at the cell monolayer is zero, neighbor nodes were used to perform the calculation of shear stress to obtain a multidimensional velocity gradient. By defining five concentric rings (R) numbered R1 through R5, each with a ring width of $185 \mu\text{m}$, computational modeling demonstrated that the magnitude of shear stress increased with each concentric ring before reaching the maximum of 25.1 dyn/cm^2 in R2 before

progressively decreasing (Figure 1C). This shear stress profile corresponded to a converging shear stress gradient (increases with positive distance from flow source) from R0–R2 and a negative shear stress gradient (decreases with positive distance from the flow source) from R3–R5.

Using this device, ECs cultured on randomly oriented or aligned nanofibrillar films were exposed to a spatial gradient in wall shear stress to examine its effect on EC morphology, alignment, and motility. After 24 h, the orientation of cells on randomly oriented collagen was quantified using a custom Matlab program and the cells were pseudocolored based on their orientation as being parallel (blue), orthogonal (red), or intermediate (green) relative to a radial axis (Figure 2A,B). The

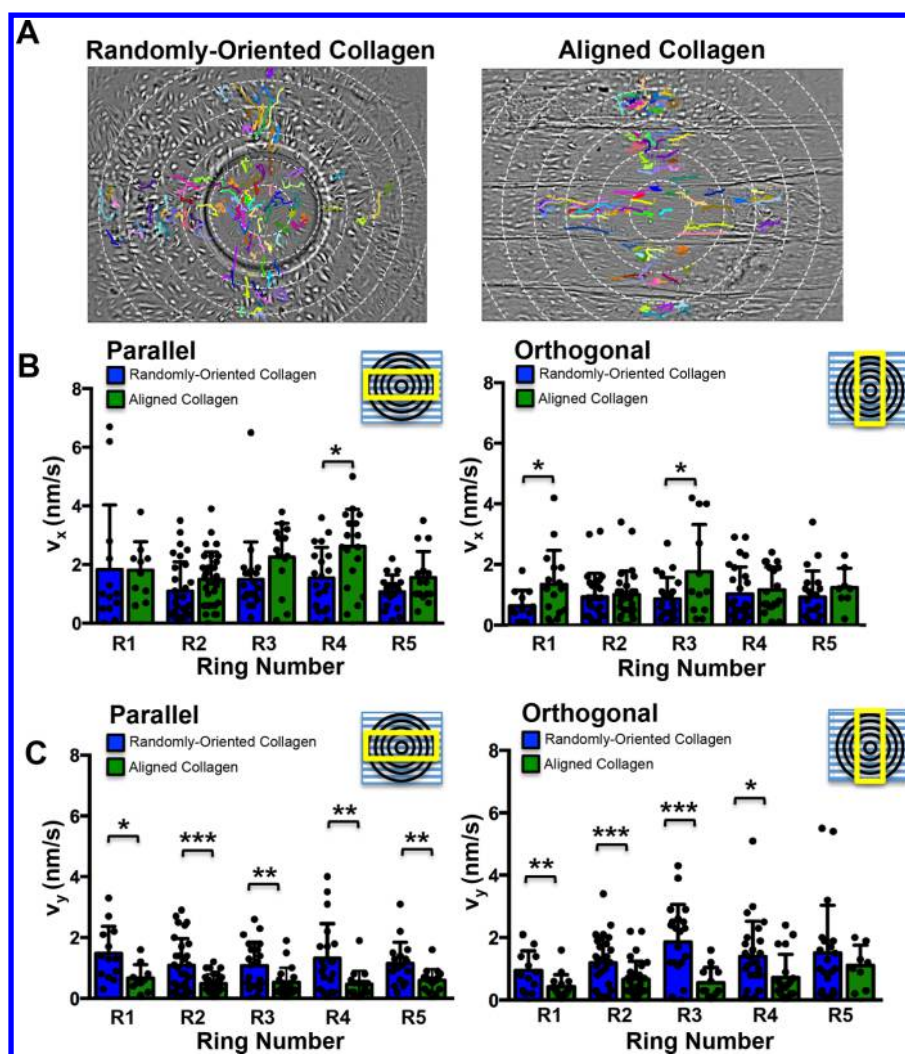


Figure 3. Migration trajectories on aligned nanofibrillar films after exposure to spatially varying shear stress magnitudes show preferential migration patterns. (A) Representative images showing the migration pathways of individual cells during 24 h of disturbed flow when cultured on randomly oriented or aligned nanofibrillar films. White dotted circles denote the boundaries of each ring experiencing distinct regions of the shear gradient. (B) The mean migration velocities (x -component, v_x) of cells within each ring on randomly oriented or aligned nanofibrillar films at parallel or orthogonal regions. (C) The mean velocities (y -component, v_y) for each ring on randomly oriented or aligned nanofibrillar films at parallel or orthogonal regions. Inset shows a parallel or orthogonal region represented by each graph. Data are shown based on three samples per group out of at least 20 cells per ring. * $p < 0.05$, ** $p < 0.01$, *** $p < 0.001$.

distribution of cellular orientations was further arranged in a rosette histogram for each ring to show the distribution and frequency of cell alignment in polar coordinates. As shown in Figure 2C, the cellular orientations were generally distributed throughout the range of 0 – 90° with no preferential orientation in rings of varying magnitudes of shear stress (R1–R5). After 24 h of exposure to varying shear stress magnitudes, the distribution of cellular orientations remained in a random distribution (Figure S2a, Supporting Information).

In contrast to ECs seeded on randomly oriented films, the ECs seeded on aligned nanofibrillar films were highly oriented along the direction of the nanofibrils prior to shear stimulation (Figure S2b, Supporting Information) and remained oriented along the direction of the nanofibrils after 24 h of exposure to shear stress (Figure 2D,E). The cellular orientations were plotted in Cartesian coordinates, relative to a horizontal axis, because preferential cell alignment in the direction of the nanofibrils was masked in polar coordinates (Figure S3, Supporting Information). As shown by the pseudocolored

cells and rosette histograms, the majority of the cells had angles of alignment of 0 – 15° (dark blue) indicating that the cells preferentially oriented along the axis of the nanofibrils, and this aligned orientation was maintained consistently across all five rings, even in regions in the rings where cells were exposed to shear orthogonal to the direction of cellular orientation (Figure 2F). These data demonstrate that ECs remained aligned along the direction of the nanofibrils, even when exposed to shear oriented orthogonal to the direction of the nanofibrils.

To further characterize the differences in cellular elongation after shear stimulation, the cell shape index (CSI) was calculated for each ring based on F-actin staining. Notably, the average CSI of ECs on aligned nanofibrillar films was significantly lower compared to ECs on randomly oriented films for all rings (that is, 0.66 ± 0.17 randomly oriented versus 0.41 ± 0.12 on aligned sample in R2, $p < 0.001$), indicating that the ECs on aligned nanofibrillar films were more elongated in morphology (Figure S4a,b, Supporting Information). This difference in CSIs for cells on randomly oriented versus aligned

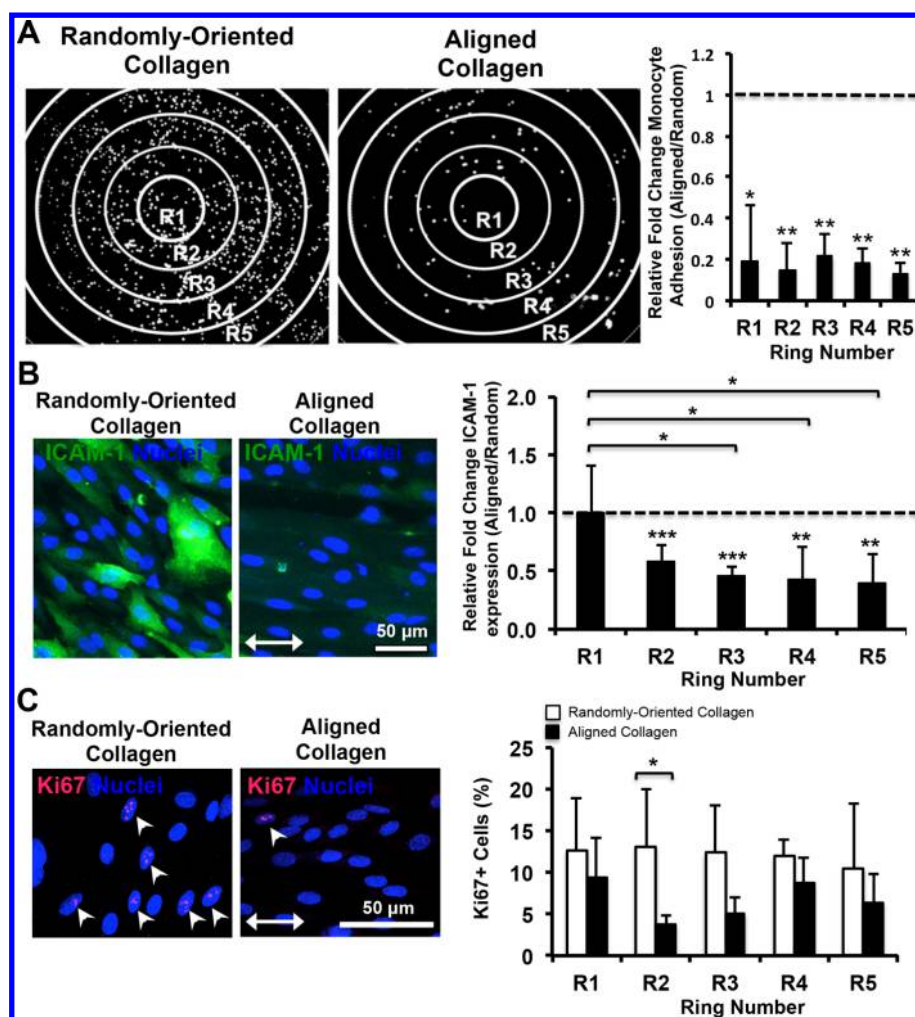


Figure 4. ECs cultured on aligned nanofibrillar films retain anti-inflammatory properties despite exposure to spatially varying shear stress. (A) Adhesion of fluorescently labeled monocytes onto an EC monolayer after exposure to disturbed flow on either randomly oriented or aligned films. White circles denote the boundaries for each ring. Graph (far right) represents relative fold change of adhered monocytes onto ECs on aligned nanofibrillar vs randomly oriented films. (B) ICAM-1 expression by ECs on randomly oriented or aligned collagen. The graph (far right) shows the relative fold change in ICAM-1 expression on aligned nanofibrillar films. Dotted line denotes the relative value of one of the randomly oriented samples. Representative images taken from R2. (C) Ki67 expression as a marker of proliferation on randomly oriented or aligned nanofibrillar collagen films. Arrows denote Ki67-expressing cell nuclei. The graph (far right) shows the percentage of Ki67-expressing cells for each ring. Data are shown based on three samples per group out of at least 20 cells per ring. Representative images are shown from R2. * $p < 0.05$, ** $p < 0.01$, *** $p < 0.001$.

collagen films was statistically significant for cells in all rings ($p < 0.001$). Together, these data demonstrate that even when shear was orthogonal to EC orientation, ECs on aligned nanofibrillar films retained their elongated cell shape along the direction of the nanofibrils.

Automated live cell imaging was used to assess cell motility at regions of rings that were either parallel (congruent) or orthogonal (opposing) to the direction of the aligned nanofibrils (Figure S5, Supporting Information). Compared to ECs on randomly oriented nanofibrils, ECs on aligned nanofibrils moved predominately along the axis of the collagen nanofibrils, designated as the x -axis (Figure 3A, Movies S1 and S2, Supporting Information). In parallel regions in R4, ECs on the aligned nanofibrillar films migrated at an almost 2-fold greater velocity in the x -component (v_x), compared to ECs on randomly oriented films (1.5 ± 1.1 nm/s on randomly oriented films versus 2.8 ± 1.3 nm/s on aligned nanofibrillar films, $p < 0.05$) (Figure 3B). Strikingly, even when flow-induced shear was directed orthogonally to the direction of aligned nano-

fibrils, ECs cultured on the aligned nanofibrillar films migrated at significantly faster v_x than those on the randomly oriented films (R1, 0.6 ± 0.5 nm/s on randomly oriented films versus 1.3 ± 1.1 nm/s on aligned films; R3, 0.9 ± 0.7 nm/s on randomly oriented films versus 1.8 ± 1.5 nm/s on aligned films; $p < 0.05$). Conversely, v_y was consistently lower on aligned nanofibrillar films compared to that on randomly oriented films in R1–R4 at both the parallel ($p < 0.05$, $p < 0.001$, $p < 0.001$, $p < 0.01$, respectively) and orthogonal regions (Figure 3c, $p < 0.05$, $p < 0.001$, $p < 0.001$, $p < 0.05$, respectively). To rule out the possibility that aligned nanofibrillar films prevented cell migration, the total distance traveled by each cell was quantified and shown to be similar on both randomly oriented and aligned nanofibrillar films (Figure S6, Supporting Information). Additionally, despite the inflection of shear stress gradient at R2 (Figure 1C), there were no significant differences in migration velocity when cells were exposed to positive shear gradients (R1,R2), in comparison to negative shear gradients (R3–R5). Together, these data suggest that parallel-aligned

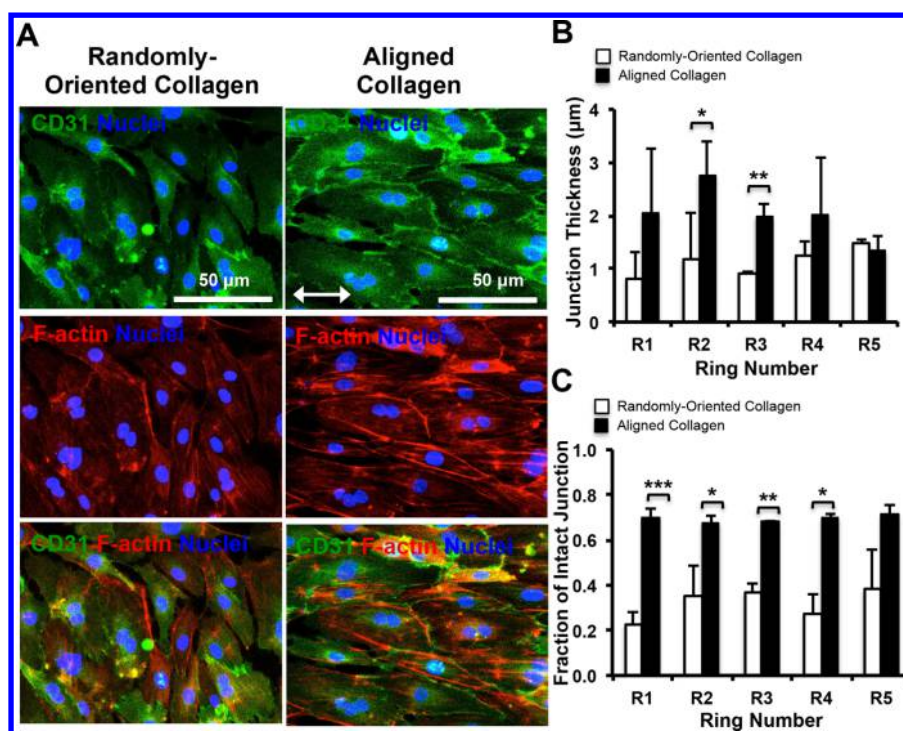


Figure 5. Aligned spatial patterning modulates CD31 junction thickness and organization despite exposure to spatially varying shear stress. (A) CD31 localization in cells adhering to randomly oriented (left) or aligned nanofibrillar collagen (right). F-actin marks the cytoskeletal perimeter. Representative images taken from R2. (B) Junction thickness for each ring. (C) Colocalization of F-actin and CD31 was used to quantify the fraction of intact junctions (fraction of cell boundary marked with CD31). Data are shown based on three samples per group out of at least 20 cells per ring. * $p < 0.05$, ** $p < 0.01$, *** $p < 0.001$.

cells were able to resist changes in cellular morphology and motility, even when flow-induced shear was directed orthogonally to the direction of cell patterning.

Within straight segments of blood vessels, ECs align along the orientation of laminar blood flow, and these cells are functionally able to resist atherosclerotic lesion formation by inhibiting adhesion of lipogenic proteins and monocytes in the circulating blood.¹⁶ To determine whether cell patterning derived from aligned nanofibrillar films could abrogate inflammation as an early event in the process of atherosclerosis, ECs on aligned or randomly oriented films were exposed to varying shear stress magnitudes for 24 h followed by incubation with fluorescent monocytes. Interestingly, a 5-fold reduction of monocyte adhesion to ECs was observed for all rings on the aligned nanofibrillar films, compared to randomly oriented cells, after 24 h of shear (Figure 4A, $p < 0.05$). Furthermore, the reduction in monocyte adhesion was observed in regions where the shear direction was parallel as well as where it was orthogonal to the direction of aligned nanofibrils, suggesting that aligned spatially patterned ECs could resist monocyte adhesion regardless of the direction of shear (Figure S7, Supporting Information). Together, our data suggest that ECs on aligned nanofibrillar films could maintain anti-inflammatory function, even in the presence of varying spatial shear stress magnitudes, regardless of the direction of shear relative to cellular orientation.

During the early stages of atherosclerotic lesion formation, inflammation-related adhesion molecules such as intercellular adhesion molecule-1 (ICAM-1) are upregulated at the endothelial surface and function to recruit and bind monocytes.¹⁷ To verify the finding that aligned patterning of ECs supported reduced monocyte adhesion, we further

quantified the expression level of ICAM-1. Indeed, ICAM-1 expression by ECs on aligned nanofibrillar films was 2-fold lower than that of cells on randomly oriented films in R2-R5 (Figure 4B, $p < 0.01$) but not significantly different in R1. In comparing ICAM-1 expression at regions in which shear was parallel versus orthogonal to the aligned nanofibril direction, ICAM-1 expression was consistently lower for ECs cultured on aligned nanofibrillar films, compared to monocyte adhesion on randomly oriented nanofibrillar films (Figure S8a, Supporting Information). These data suggested that ICAM-1 expression was markedly abrogated in ECs on aligned nanofibrillar films, regardless of whether shear was parallel or orthogonal to the direction of aligned nanofibril orientation.

Vascular trauma or disease increases the rate of EC turnover (apoptosis and proliferation). However, when the repair of the damaged endothelium is inadequate, pathologic diseases including atherosclerosis and other ischemic conditions can arise.¹⁸ In physiological regions of disturbed flow, nonorganized EC morphology is associated with the production of pro-thrombotic gene products and increases in EC proliferation and apoptosis, resulting in high EC turnover.⁸ Therefore, we compared the effects of disturbed flow resulting from spatially varying wall shear stress on EC proliferation (Figure 4C). By immunofluorescently staining for Ki67, a proliferation-associated nuclear protein that is expressed during active phases of the cell cycle (G1, S, G2, and mitosis) but is absent from resting cells (G0), we showed that ECs on aligned nanofibrillar films in R2 had a 3-fold reduction in Ki67 expressing cells, compared to those on randomly oriented films ($p < 0.05$). Specifically, the greatest reduction in Ki67 expression was observed in the R2 and R3 regions ($p < 0.05$) in which shear was orthogonal to the aligned nanofibril direction (Figure S8b,

Supporting Information). These data further support our finding that ECs aligned by spatially patterned films could resist the progression of atherosclerosis by abrogating inflammation as well as reducing EC turnover in the presence of disturbed flow.

Besides intracellular changes, we also examined cell–cell junction thickness and organization, because intercellular junctions are critical for endothelial barrier function.^{19,20} Immunofluorescence staining for CD31 (PECAM-1), a cell adhesion molecule that associates with intercellular junctions demonstrated significantly thicker junctions in cells cultured on aligned nanofibrillar films, in comparison to those on randomly oriented films (Figure 5A). The greatest differences were observed in R2–R3 with a 2-fold increase in junction thickness on aligned collagen films (Figure 5B) ($p < 0.05$ for R2; $p < 0.01$ for R3). Intriguingly, the EC junctions also appeared to be more intact after exposure to shear stress when cultured on aligned films as compared to randomly oriented films (Figure 5C). The fraction of intact EC junctions was 2–3-fold greater on aligned films compared to randomly oriented films ($p < 0.001$ for R1; $p < 0.05$ for R2; $p < 0.01$ for R3; $p < 0.05$ for R4), suggesting that spatial nanopatterning may be a modulator of not only junction thickness but also junction integrity.

Blood vessels are comprised of fibrillar ECMs at the nano- and microscale.² Nanopatterning of advanced functional biomaterials, therefore, enables systematic studies of cell–ECM interactions in physiologically relevant length scales. It is only once ECM features reach biomimetic length scales (<200 nm) that many common cellular behaviors such as adhesion and proliferation can be modulated with topography.²¹ Unlike other patterning-based approaches such as topographically patterned microchannels that restrict cellular alignment by limiting the degrees of freedom to move,^{22,23} our nanofibrillar films have much smaller fibril diameters of 30–50 nm that do not confine cell alignment along the direction of nanopatterning, suggesting that cells orient along the nanofibrils by preference.

Although the shear-based fibrillogenesis method described in the current study is unique to collagen, other approaches for fabrication of nanofibrillar biomaterials have been demonstrated. One approach involves the use of anodized aluminum oxide nanopores to extrude individual fibronectin fibers with nanometer diameters.²⁴ In another approach, shear force was applied to a sheet of globular fibronectin at the air–liquid interface along an array of elastic micropillars to drive fibronectin fiber assembly, producing smooth fibronectin fibers with 14 nm diameters.^{25,26} Future studies are warranted to determine whether the findings from nanofibrillar collagen films may be applicable to other ECMs.

The role of nanofibrillar cues in modulating cell phenotype and function has been documented.^{27,28} However, the fundamental signaling mechanisms are not well understood. Recent papers suggest important roles of nanotopographical substrates in inducing activation and clustering of transmembrane integrin receptors that bind to ECM substrates.²⁹ Compared to cell bodies, individual integrin transmembrane receptors are similar in size to nanoscale topographical features.⁸ Feetlike cellular extensions called filipodia can experience contact guidance from topographical features as small as 10 nm in height and some cellular “nanopodia” have the ability to respond to features below the 10 nm range.^{30,31} Consequently, nanopatterned materials allow for sensitive tuning of mechanotransduction pathways through integrin

receptors, enabling more direct modulation of receptor-mediated mechanosensitive pathways.¹ Since integrin activation is also a known mediator of downstream inflammation-related pathways,³² it is possible that subunit-specific integrin activation on aligned nanofibrillar films may precondition ECs toward an anti-inflammatory state.

To demonstrate the role of cell patterning in modulating EC function, we utilized nanofibrillar ECMs that induce parallel alignment of ECs to mimic cell morphology within straight vessel segments, which have reduced inflammation. We showed that ECs prealigned using nanofibrillar substrates remain oriented along the direction of the nanofibrils, even in the presence of orthogonal flow-induced shear stress. Furthermore, even when exposed to orthogonal flow-induced shear stress, ECs prealigned by nanofibrillar substrates exhibited anti-inflammatory characteristics and reduced disruption of adhesion junctions, when compared to ECs grown on randomly oriented collagen. Others have shown that ECs prealigned by flow-induced laminar shear stress readily reorient their long axis along the direction of fluid flow when subjected to a directional change in shear stress.³³ This morphological change was also accompanied by increased activation of the pro-inflammatory marker NF- κ B when subjected to shear stress orthogonal to the direction of the cell's long axis.³⁴ The difference in findings may be due to differential activation of signaling pathways, since nanotopographical cues more closely approximate the size of focal adhesion complexes (integrin spacing of approximately 45 nm) that relay ECM cues from the extracellular environment to the cytoskeleton.³⁵ In addition, differences in the chemical composition of the ECM substrates may play a role. Since collagen I fibers reduce global fibronectin fiber strain by mechanically stabilizing fibronectin fibrils as a result of a conformation-dependent interaction between the binding domains of these two ECM proteins,³⁶ it is plausible that ECM differences in force-regulated integrin binding are linked to differential mechanosensitive inflammatory molecular cues and signaling pathways. Finally, the use of ICAM-1 instead of NF- κ B from previous papers may account for differences in results.³⁴ Further studies to identify the mechanism by which nanotopography modulates endothelial function under shear stress are warranted.

In the current study, spatially varying shear stress magnitudes generally showed subtle influences in endothelial function and morphology. The most prominent effect of varying shear stresses was in ICAM-1 expression, which was most pronounced in ECs located in R1 in randomly oriented films. Contributing to the elevated levels of ICAM-1 could be the presence of a stagnation point as well as a positive shear stress gradient (increasing shear stress with positive distance from the stagnation point). Others have demonstrated that positive shear gradients increase proliferation and apoptosis (programmed cell death), whereas negative gradients (decreasing shear stress with positive distance) attenuate them.³⁷ Although our studies did not show significant differences in proliferation and apoptosis between positive (R1–R2) and negative (R3–R5) shear stress gradients, this may be due to the presence of nanoscale signaling cues in our studies.

In summary, the salient findings from this study are that aligned nanofibrillar films: (1) maintain EC elongation and migration along the direction of nanopatterning, even in the presence of orthogonal flow-induced shear stress gradients; (2) abrogate inflammatory response and EC turnover; and (3) modulate CD31 junction thickness and organization to better

mimic healthy junctions. This work provides new insight into the importance of nanoscale interactions in modulating EC function in the presence of shear stress and complex fluid flow. Furthermore, our findings reveal an important interplay between cellular patterning and shear stress in maintaining EC health. These results have important implications in understanding the pathobiology of atherosclerosis and can be applied toward engineering of nanopatterned polymers as bypass grafts.

Methods. EC Culture on Parallel-Aligned Nanofibrillar Collagen Films. We have previously described the fabrication of nanofibrillar-aligned collagen films using high concentration rat tail collagen-type I (10 mg/mL in 0.02 N in acetic acid, pH 3.5, Corning) that was further dialyzed to 30 mg/mL using a semipermeable cellulose dialysis tubing of pore size 4.8 nm in diameter (Thermo Fisher) and polyethylene glycol (Sigma).³⁸ Aligned nanofibrillar collagen strips were extruded from 22G blunt tip needles at a rate of 3.2 mL/min at a velocity of 340 mm/s directly in warm pH neutral buffer (10× phosphate buffered saline, PBS, pH 7.4) to initiate fibrillogenesis immediately as the collagen is deposited. Randomly oriented collagen strips were similarly made by extrusion at a reduced velocity of 50 mm/s and an extrusion rate of 0.02 mL/min, based on our previous publication.³⁸ Once fibrillogenesis was completed, several collagen strips were attached onto glass coverslips to create a continuous film. The films were allowed to dry overnight, and then the glass coverslips were attached to 6-well #1.5 glass bottom dishes (In Vitro Scientific). The nanostructure and fibril alignment of the films were visualized by scanning electron microscopy, as described previously.^{38,39} For in vitro studies, randomly oriented or aligned nanofibrillar films were sterilized with 70% ethanol and rehydrated with 1× PBS for 2 h. Primary human dermal microvascular ECs (5×10^5) (Lonza, P7–10) were seeded onto the collagen film in EGM-2MV growth media (Lonza) at 37 °C and 5% CO₂ until they reached approximately 80% confluence.

Disturbed Flow System. A disturbed flow system resulting from spatial wall shear stress gradients was previously characterized¹⁵ to recapitulate the pathologic flow profile seen at the bifurcation points of blood vessels (Figure 1A). A Nikon TE-2000 inverted microscope with a motorized stage and enclosed in a plexiglass chamber, maintained at 37 °C, housed the cells and flow orifice. A nine-roller dampened peristaltic pump (Idex) was used to deliver cell culture media at a flow rate of 3 mL/min through 1.3 mm (inner diameter) tubing corresponding to a fluid velocity range of 0–75.3 mm/s. Media flowed downward from the flow orifice (0.7 mm inner diameter) at the conserved flow rate of 3 mL/min onto EC-cultured collagen films, corresponding to a fluid velocity range between 0 and 259.8 mm/s and producing a shear stress range of 0–25.1 dyn/cm² on the cell monolayer (Figure 1B,C), which is within physiological range.⁴⁰ Cells were exposed to disturbed flow for 24 h. Phase contrast images were collected every 25 min using Fiji software for 24 h. All images were bandpass filtered in ImageJ to increase the contrast of cell boundaries. To assess shear gradients, the cell monolayer was assigned five regions of interest, defined by concentric rings (R1, R2, R3, R4, and R5), each with a radius of 185 μm. The stagnation point, directly underneath the flow orifice, corresponded to the center of R1 where the cells experience zero shear stress. The magnitude of the shear stress increased radially outward from the jetting center with the maximum shear stress peaking within R2 (Figure 1C). The shear stress decreased from R3 to R5. The

impinging flow was modeled by axisymmetric flow using the commercial finite-element analysis (FEA) package COMSOL Multiphysics 3.5a following our previous study.¹⁵ A flow rate of 3 mL/min was prescribed at the orifice inlet and a pressure boundary condition was used at the outlet. A “no slip” boundary condition was assumed at the wall (where $z = 0$ at the cell monolayer) such that the velocity of the fluid directly at the wall is zero. The wall shear stress, τ_w , was calculated as a function of the velocity gradient, $(\partial u/\partial z)$, which quantifies how quickly fluid velocity (u) changes along the z -direction, and the fluid viscosity (μ):

$$\tau_w = \mu \left. \frac{\partial u}{\partial z} \right|_{z=0}$$

Quantification of Cellular Alignment. Cellular alignment was assessed using custom Matlab software to quantify cell orientation relative to either polar axes for randomly oriented samples (Figure 2A–C) or Cartesian axes for nanoaligned samples (Figure 2D–F). EC orientation was used to generate a rosette histogram showing the distribution of alignment angle for each ring.¹⁵ For randomly oriented films, cell orientation was quantified in polar coordinates with a range from 0° (cellular alignment parallel to radial axis) to 90° (cell alignment orthogonal to radial axis). For aligned nanofibrillar films, cell orientation was quantified in Cartesian coordinates relative to the axis of the nanofibrils, with a range from 0° (cellular alignment parallel to nanofibrils) to 90° (cell alignment orthogonal to nanofibril orientation). Cells were pseudocolored according to their angular alignment: highly aligned, dark blue (0°–15°) and medium blue (16°–30°); intermediate alignment, light blue (31°–45°) and green (46°–60°); orthogonal orientation, orange (61°–75°) and red (76°–90°). All detectable cells were quantified for each ring out of $n = 4$ samples.

Assessment of Cell Shape Index (CSI) and Proliferation. After 24 h of exposure to shear stress, the samples were fixed in 4% paraformaldehyde (Alfa Aesar), permeabilized in 0.5% Triton-X100 (Sigma), and blocked in 1% bovine serum albumin (Sigma). For staining of actin, samples were incubated with Alexa Fluor-488-conjugated phalloidin (Life Technologies). For assessment of proliferation, fixed samples were incubated with cell cycle marker Ki67 (Millipore) for 16 h at 4 °C followed by Alexa Fluor-594 antibody (Life Technologies). Samples were then counterstained with Hoechst 33342 to visualize nuclei and imaged under a fluorescence microscope or Zeiss LSM700 confocal microscope. As an indicator of cell elongation, the CSI was calculated as $CSI = 4\pi \text{ area}/\text{perimeter}^2$ from F-actin-stained ECs using the ImageJ area tool. A value of 1 corresponded to the shape of a rounded cell (circle), whereas a value of 0 depicts an elongated cell (line). For quantification of proliferation, the ImageJ particle analysis tool was used to identify the percent Ki67-expressing nuclei at parallel and orthogonal regions of each ring. At least 20 cells were quantified for each ring out of $n = 3$ samples (100 cells per sample).

Migration Trajectories. To track migration trajectories of cells on randomly oriented and aligned nanofibrillar films, timelapse microscopy was used. Phase contrast 10× images were taken every 25 min for 24 h. The movement of the cells was manually tracked using the MTrackJ plugin and used to generate vector plots that depict cell motility (Figure 3A). Migration distances and velocities were calculated in Excel and

graphed using GraphPad Prism version 6.0. At least 20 cells were quantified for each ring out of $n = 3$ samples (100 cells per sample).

Monocyte Adhesion and ICAM-1 Expression. To assess the protective effects of aligned nanofibrillar films in resisting atherosclerosis by modulating EC orientation, 5×10^6 human monocytes (U937, ATCC) prelabeled with Cell Tracker Red CMPTX (Life Technologies) were allowed to adhere onto EC-seeded randomly oriented or aligned films after 24 h of exposure to varying shear stress magnitudes. After 30 min in the presence of gentle agitation, unbound monocytes were removed with PBS, and adherent monocytes were quantified from $10\times$ images taken with a fluorescent microscope. To validate monocyte adhesion results, samples were also stained with ICAM-1 (CD54, BD Bioscience), followed by Alexa Fluor-488 secondary antibody and Hoechst 33342. ICAM-1 intensity was computed from $20\times$ confocal images and then using ImageJ's area tool to calculate the integrated density for 20 cells within each ring out of $n = 3$ samples (100 cells per sample). Data are expressed as the fold change in ICAM-1 intensity on aligned nanofibrillar films, relative to values obtained from the corresponding random sample.

Intercellular Junction Thickness. For assessment of cell junction organization, the expression of CD31,⁴¹ an endothelial adhesion protein that associates with adherens junctions, was immunofluorescently stained to visualize intercellular junctions. After 24 h of exposure to shear stress, samples were fixed, permeabilized, and blocked as described above. CD31 (Dako) primary antibody was applied, followed by AlexaFluor-488 secondary antibody and counterstained with Hoechst 33342. Images ($20\times$) were taken and converted to 8-bit grayscale for analysis. Junction thickness was calculated based on previous publications in which the ImageJ line tool was used to draw a line (1 pixel \times 50 pixels) orthogonal to three prominent regions of a cell's junction perimeter (Figure S9a, [Supporting Information](#)).^{19,42} An intensity profile of the grayscale values was obtained for each measurement. Each profile exhibited two distinct Gaussian curves, where the peaks represented the clustering of junctional proteins at the edges of each cell. The distance between the two intensity maxima was measured as the minimal gray value that exceeded all peaks due to noise (Figure S9b, [Supporting Information](#)). Pixels measured from the intensity plot were converted to equivalent pixels on the CD31 image and then to microns. The average of three measurements was taken as the junction thickness of a given cell. The junction completeness was determined by visualizing the cell perimeter using F-actin staining and then measuring the percent of the perimeter that expressed CD31. Briefly, the total length of the cell perimeter was measured using the F-actin-stained images and ImageJ's perimeter tool (Figure S9c, [Supporting Information](#)). The total length of all the CD31+ junctions for the corresponding cell was measured with ImageJ's line tool (Figure S9d, [Supporting Information](#)). The completeness of the junction was calculated as the percent of the total perimeter length colocalized with CD31 expression. Only cells with cell–cell contact on all sides were counted. For junction thickness and junction completeness analysis, at least 20 cells were quantified for each ring out of $n = 3$ samples (100 cells per sample).

Statistical Analysis. In all assays, data are averaged from $n \geq 3$ samples and data are shown as mean \pm standard deviation. Proliferation, monocyte adhesion data, ICAM-1, and junction measurements are expressed as mean data per sample.

Migration trajectory, migration distances, and CSI are expressed as mean data per cell. Statistical analysis was performed by GraphPad Prism version 6.0. Statistical significance was determined using an unpaired two-tailed student's t-test in which statistical significance was accepted at $p < 0.05$. Where noted, * denotes $p < 0.05$, ** denotes $p < 0.01$, and *** denotes $p < 0.001$.

■ ASSOCIATED CONTENT

📄 Supporting Information

The Supporting Information is available free of charge on the ACS Publications website at DOI: [10.1021/acs.nanolett.5b04028](https://doi.org/10.1021/acs.nanolett.5b04028).

Characterization of nanofibrillar films, EC culture on films under static conditions; quantification of intercellular junction thickness and completeness; comparison of parallel versus orthogonal regions in analysis of proliferation, monocyte adhesion, and ICAM-1 expression ([PDF](#))

Migration on randomly oriented collagen ([AVI](#))

Migration on aligned collagen ([AVI](#))

■ AUTHOR INFORMATION

Corresponding Author

*E-mail: ngantina@stanford.edu. Tel: (650) 849-0559. Fax: (650) 725-3846.

Notes

The authors declare no competing financial interest.

■ ACKNOWLEDGMENTS

This study was supported in part by grants to NFH from the U.S. National Institutes of Health (R00HL098688 and EB020235-01), Merit Review Award (1I01BX002310) from the Department of Veterans Affairs Biomedical Laboratory Research and Development, the Stanford Chemistry Engineering and Medicine for Human Health, and the Stanford Cardiovascular Institute. This study was supported in part by a grant to ARD and GGF from the National Institutes of Health (R01HL128779-01). K.H.N. was supported by postdoctoral fellowships from the National Institutes of Health (1T32HL098049) and the American Heart Association (15POST25560045).

■ REFERENCES

- (1) Rosso, F.; Giordano, A.; Barbarisi, M.; Barbarisi, A. *J. Cell. Physiol.* **2004**, *199* (2), 174–80.
- (2) Stehbens, W. E.; Martin, B. J. *Connect. Tissue Res.* **1993**, *29* (4), 319–31.
- (3) Kim, D. H.; Provenzano, P. P.; Smith, C. L.; Levchenko, A. *J. Cell Biol.* **2012**, *197* (3), 351–60.
- (4) Huang, N. F.; Okogbaa, J.; Lee, J. C.; Jha, A.; Zaitseva, T. S.; Paukshto, M. V.; Sun, J. S.; Punjya, N.; Fuller, G. G.; Cooke, J. P. *Biomaterials* **2013**, *34* (16), 4038–47.
- (5) Huang, N. F.; Lai, E. S.; Ribeiro, A. J.; Pan, S.; Pruitt, B. L.; Fuller, G. G.; Cooke, J. P. *Biomaterials* **2013**, *34* (12), 2928–37.
- (6) Dai, G.; Kaazempur-Mofrad, M. R.; Natarajan, S.; Zhang, Y.; Vaughn, S.; Blackman, B. R.; Kamm, R. D.; Garcia-Cardena, G.; Gimbrone, M. A., Jr. *Proc. Natl. Acad. Sci. U. S. A.* **2004**, *101* (41), 14871–6.
- (7) Chiu, J. J.; Chien, S. *Physiol. Rev.* **2011**, *91* (1), 327–87.
- (8) Hahn, C.; Schwartz, M. A. *Nat. Rev. Mol. Cell Biol.* **2009**, *10* (1), 53–62.
- (9) Chien, S. *Ann. Biomed. Eng.* **2008**, *36* (4), 554–62.

- (10) Chiu, J.-J.; Usami, S.; Chien, S. *Ann. Med.* **2009**, *41* (1), 19–28.
- (11) Li, S.; Huang, N. F.; Hsu, S. *J. Cell. Biochem.* **2005**, *96* (6), 1110–26.
- (12) Cooke, J. P. *Proc. Natl. Acad. Sci. U. S. A.* **2003**, *100* (3), 768–70.
- (13) Chien, S. *Am. J. Physiol. Heart Circ. Physiol.* **2006**, *292* (3), H1209–H1224.
- (14) Lloyd-Jones, D.; Adams, R. J.; Brown, T. M.; Carnethon, M.; Dai, S.; De Simone, G.; Ferguson, T. B.; Ford, E.; Furie, K.; Gillespie, C.; Go, A.; Greenlund, K.; Haase, N.; Hailpern, S.; Ho, P. M.; Howard, V.; Kissela, B.; Kittner, S.; Lackland, D.; Lisabeth, L.; Marelli, A.; McDermott, M. M.; Meigs, J.; Mozaffarian, D.; Mussolino, M.; Nichol, G.; Roger, V. L.; Rosamond, W.; Sacco, R.; Sorlie, P.; Roger, V. L.; Thom, T.; Wasserthiel-Smoller, S.; Wong, N. D.; Wylie-Rosett, J. *Circulation* **2010**, *121* (7), e46–e215.
- (15) Ostrowski, M. A.; Huang, N. F.; Walker, T. W.; Verwijlen, T.; Poplawski, C.; Khoo, A. S.; Cooke, J. P.; Fuller, G. G.; Dunn, A. R. *Biophys. J.* **2014**, *106* (2), 366–74. Ostrowski, M. A.; Huang, E. Y.; Surya, V. N.; Poplawski, C.; Barakat, J. M.; Lin, G. L.; Fuller, G. G.; Dunn, A. R. *Ann. Biomed. Eng.* **2015** DOI: [10.1007/s10439-015-1500-7](https://doi.org/10.1007/s10439-015-1500-7).
- (16) Eagle, K. A.; Guyton, R. A.; Davidoff, R.; Ewy, G. A.; Fonger, J.; Gardner, T. J.; Gott, J. P.; Herrmann, H. C.; Marlow, R. A.; Nugent, W. C.; O'Connor, G. T.; Orszulak, T. A.; Rieselbach, R. E.; Winters, W. L.; Yusuf, S.; Gibbons, R. J.; Alpert, J. S.; Eagle, K. A.; Garson, A., Jr.; Gregoratos, G.; Russell, R. O.; Smith, S. C., Jr. *J. Am. Coll. Cardiol.* **1999**, *34* (4), 1262–1347.
- (17) Kaplanski, G.; Marin, V.; Fabrigoule, M.; Boulay, V.; Benoliel, A. M.; Bongrand, P.; Kaplanski, S.; Farnarier, C. *Blood* **1998**, *92* (4), 1259–67.
- (18) Takabe, W.; Alberts-Grill, N.; Jo, H. *J. Cell Biol.* **2011**, *193* (5), 805–7.
- (19) Seebach, J.; Donnert, G.; Kronstein, R.; Werth, S.; Wojciak-Stothard, B.; Falzarano, D.; Mrowietz, C.; Hell, S. W.; Schnittler, H. J. *Cardiovasc. Res.* **2007**, *75* (3), 596–607.
- (20) Miao, H.; Hu, Y. L.; Shiu, Y. T.; Yuan, S.; Zhao, Y.; Kaunas, R.; Wang, Y.; Jin, G.; Usami, S.; Chien, S. *J. Vasc. Res.* **2005**, *42* (1), 77–89.
- (21) Liliensiek, S. J.; Nealey, P.; Murphy, C. J. *Tissue Eng., Part A* **2009**, *15* (9), 2643–51.
- (22) Sun, Y.; Weng, S.; Fu, J. *Wiley Interdiscip. Rev. Nanomed. Nanobiotechnol.* **2012**, *4* (4), 414–27.
- (23) Gray, B.; Lieu, D.; Collins, S.; Smith, R.; Barakat, A. *Biomed. Microdevices* **2002**, *4* (1), 9–16.
- (24) Raoufi, M.; Das, T.; Schoen, I.; Vogel, V.; Bruggemann, D.; Spatz, J. P. *Nano Lett.* **2015**, *15* (10), 6357–64.
- (25) Kaiser, P.; Spatz, J. P. *Soft Matter* **2010**, *6*, 113–119.
- (26) Ulmer, J.; Geiger, B.; Spatz, J. P. *Soft Matter* **2008**, *4*, 1998–2007.
- (27) Dalby, M. J.; Gadegaard, N.; Tare, R.; Andar, A.; Riehle, M. O.; Herzyk, P.; Wilkinson, C. D.; Oreffo, R. O. *Nat. Mater.* **2007**, *6* (12), 997–1003.
- (28) McMurray, R. J.; Gadegaard, N.; Tsimbouri, P. M.; Burgess, K. V.; McNamara, L. E.; Tare, R.; Murawski, K.; Kingham, E.; Oreffo, R. O.; Dalby, M. J. *Nat. Mater.* **2011**, *10* (8), 637–44.
- (29) Dalby, M. J.; Gadegaard, N.; Oreffo, R. O. *Nat. Mater.* **2014**, *13* (6), 558–69.
- (30) Dalby, M. J.; Riehle, M. O.; Johnstone, H.; Affrossman, S.; Curtis, A. S. *Cell Biol. Int.* **2004**, *28* (3), 229–36.
- (31) McNamara, L. E.; Sjoström, T.; Seunarine, K.; Meek, R. D.; Su, B.; Dalby, M. J. *J. Tissue Eng.* **2014**, *5*, 2041731414536177.
- (32) Luu, N. T.; Glen, K. E.; Egginton, S.; Rainger, G. E.; Nash, G. B. *Thromb. Haemostasis* **2013**, *109* (2), 298–308.
- (33) Wang, C.; Lu, H.; Schwartz, M. A. *J. Biomech. Eng.* **2012**, *45* (7), 1212–8.
- (34) Wang, C.; Baker, B. M.; Chen, C. S.; Schwartz, M. A. *Arterioscler., Thromb., Vasc. Biol.* **2013**, *33* (9), 2130–6.
- (35) Patla, I.; Volberg, T.; Elad, N.; Hirschfeld-Warneken, V.; Grashoff, C.; Fassler, R.; Spatz, J. P.; Geiger, B.; Medalia, O. *Nat. Cell Biol.* **2010**, *12* (9), 909–15.
- (36) Kubow, K. E.; Vukmirovic, R.; Zhe, L.; Klotzsch, E.; Smith, M. L.; Gourdon, D.; Luna, S.; Vogel, V. *Nat. Commun.* **2015**, *6*, 8026.
- (37) Dolan, J. M.; Meng, H.; Singh, S.; Paluch, R.; Kolega, J. *Ann. Biomed. Eng.* **2011**, *39* (6), 1620–31.
- (38) Lai, E. S.; Huang, N. F.; Cooke, J. P.; Fuller, G. G. *Regener. Med.* **2012**, *7* (5), 649–61.
- (39) Nakayama, K. H.; Joshi, P. A.; Lai, E. S.; Gujar, P.; Joubert, L. M.; Chen, B.; Huang, N. F. *Regener. Med.* **2015**, *10* (6), 745–55.
- (40) Dewey, C. *Fluid Mechanics of Arterial Flow*; Plenum Press: New York, 1979; Vol. 115.
- (41) Ayalon, O.; Sabanai, H.; Lampugnani, M. G.; Dejana, E.; Geiger, B. *J. Cell Biol.* **1994**, *126* (1), 247–58.
- (42) Huynh, J.; Nishimura, N.; Rana, K.; Peloquin, J. M.; Califano, J. P.; Montague, C. R.; King, M. R.; Schaffer, C. B.; Reinhart-King, C. A. *Sci. Transl. Med.* **2011**, *3* (112), 112ra122.